Viscous-Inviscid Analysis of Dual-Jet Ejectors

T. S. Lund*
Joint Institute for Aeronautics and Acoustics, Stanford University, Stanford, California 94305

A viscous-inviscid interaction method is developed to predict the performance of two-dimensional, incompressible flow ejectors that use two primary jets. The flowfield is subdivided into a viscous region that contains the turbulent jets and an inviscid region that contains the ambient fluid drawn into the device. The inviscid flow is modeled with a higher-order panel method, and an integral method is used for the description of the viscous part. The strong viscous-inviscid interaction between the jets and the ambient fluid is simulated in an iterative process where the two regions influence each other en route to a converged solution. This formulation retains much of the essential physics of the problem but at the same time requires only a small amount of computing effort. The model is applied to a parametric study that illustrates the connection between the details of the ejector geometry and the level of thrust augmentation. The advantages of a dual-jet configuration are assessed through a comparison of the present results with similar calculations for an otherwise identical single-jet ejector.

Introduction

A THRUST augmenting ejector consists of one or more high momentum primary jets that are issued into the confines of an aerodynamic shroud (see Fig. 1). As the jets evolve, they entrain some of the ambient fluid contained within the ejector, thereby inducing a secondary stream to flow in through the ejector inlet. As the secondary flow is accelerated around the leading edges of the ejector shroud, it lowers the surface pressure in these regions. The resulting leading edge suctions create aerodynamic forces that have a large component in the direction of the primary nozzle thrust. These forces, together with the increased momentum flux of the primary nozzles due to the lowered pressure within the ejector, augment the force produced by the primary jets.

An important application of thrust augmenting ejectors is found in vertical and short takeoff and landing (VSTOL) aircraft, where there is a need for a large source of powered lift. Various methods including control volume,[1,2,3,4] finite difference,[5,6,7,8] and viscous-inviscid[9,10,11] approaches have been developed to aid in the design of ejectors for VSTOL applications. Each class of methods has its share of strengths and weaknesses when considered in the simultaneous light of accuracy, efficiency, range of applicability, and the number of necessary assumptions. The engineer gains the most advantage by choosing a method that is best suited for a particular configuration or design phase.

In the performance optimization environment, the viscous-inviscid approach may provide the best level of compromise between accuracy and computational efficiency. This advantage is achieved by dividing the flowfield into a viscous zone that includes the turbulent jet and an inviscid zone that contains the entrained secondary flow. Approximations are applied to each zone independently to simplify the problem while still resolving the essential flow physics. The two zones are then solved together in an iterative process that simulates the interaction of the jet with the ambient fluid. Once the iteration is complete, the flow variables are continuous at the interface between the viscous and inviscid zones.

Received May 29, 1987; presented as Paper 87-1381 at the AIAA 19th Fluid Dynamics, Plasma Dynamics and Laser Conference, Honolulu, HI, June 8-10, 1987; revision received Nov. 1, 1989.

*Research Assistant, Department of Aeronautics and Astronautics. Member AIAA.

The viscous-inviscid models developed previously have employed a variety of approximate methods for the viscous and inviscid parts. Bevilaqua and DeJoode[9] developed a method in which a vortex lattice solution for the inviscid ambient flow was matched together with a finite-difference solution for the turbulent jet. Tavella and Roberts[10] developed a viscous-inviscid model with increased efficiency by using a conformal mapping solution for the inviscid part and an integral method for the turbulent jet. Lund et al.[11] combined a higher-order panel method for the inviscid flow with an integral method for the turbulent jet to produce an algorithm that makes use of fewer approximations than those used by both Bevilaqua and Tavella.

One significant limitation of the viscous-inviscid models produced to date is that they are all restricted to a single primary jet. It has been observed experimentally[12] that ejector performance is increased significantly when more than one primary jet is used. Most modern ejector designs take advantage of this fact and employ two or more primary nozzles. There is therefore a need to produce a theoretical model capable of simulating an ejector with more than one primary nozzle.

In the present work, a viscous-inviscid model is developed to predict the performance of an ejector with two primary jets. The inviscid flow is treated with a higher-order panel method, whereas an integral method is used to describe the turbulent jet. Lateral pressure gradients that develop across the ejector duct are accounted for with an approximate transverse momentum equation that relates the pressure difference across the jets to the curvature of their centerlines. The model is limited to two-dimensional, incompressible, steady flow.

The model is used to explore the relationship between ejector geometry and performance. This is done in a parametric study where the nozzle position and orientation, ejector length, and diffuser area ratio are varied independently. Increases in performance associated with the dual-jet configuration are assessed through a comparison of the present results with the predictions of a single-jet model developed previously.[11] Finally, a comparison is made with experimental data for the thrust augmentation ratio as a function of nozzle position.

Viscous-Inviscid Approach

The flowfield is divided into viscous and inviscid zones as shown in Fig. 1. The viscous zone originates at each of the two primary nozzles and expands downstream corresponding to the actual computed jet growth rates. The inviscid zone covers the region between the two jets, between the jet and the ejector channel wall, and the space outside the ejector. The configuration is assumed to be symmetric with respect to the ejector

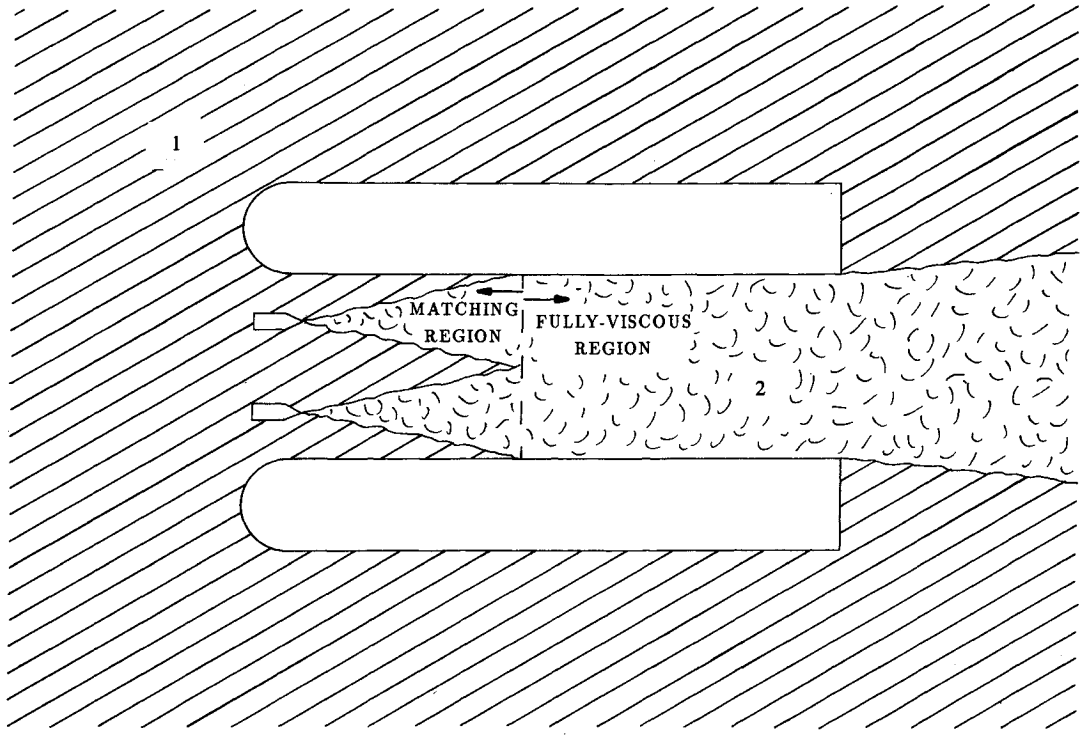

1 Inviscid zone—higher-order panel method 2 Viscous zone—integral method

Fig. 1 Thrust augmenting ejector and the viscous-inviscid approach.

channel centerline, and thus it is sufficient to model only the upper half.

Figure 1 also shows a subdivision of the viscous flow into a viscous-inviscid matching region and a fully viscous region. Within the matching region, the viscous and inviscid solutions influence each other directly through a shared boundary condition at the zonal interface. This boundary condition takes the form of the transverse component of velocity crossing the boundary and has the physical interpretation of the jet entrainment velocity. The location of the interface is also iteratively adjusted to reflect the computed jet trajectory and spreading rate.

The viscous equations alone are solved in the fully viscous region. There is still an interaction with the inviscid flow within this region, since the requirement that pressure computed at the ejector exit match the local ambient value is used to iteratively adjust the level of pressure with the inviscid portion of the ejector.

Inviscid Solution

The inviscid problem is solved within an incompressible potential flow framework. This formulation leads to Laplace's equation for the velocity potential and Bernoulli's equation for the pressure. A higher-order panel method, which has been described in detail elsewhere,[13,14] is used to obtain the solution. The higher-order scheme is needed to predict the flow within the internal region of the ejector inlet accurately. Figure 2 shows a profile of the surface over which the panels are distributed for the upper half-plane. The jet is modeled as a permeable boundary with suction applied to its surface to account for entrainment of the inviscid flow. The position of the jet and the distribution of entrainment are determined in the matching process. The lowered pressure within the ejector is simulated by applying suction to the semicircular control stations that connect the jet with the plane of symmetry and the ejector wall. The suction velocity is determined in the interaction process such that the ejector exit pressure matches the local ambient value. The ejector shroud as well as the streamline that lies along the plane of symmetry are treated as solid surfaces.

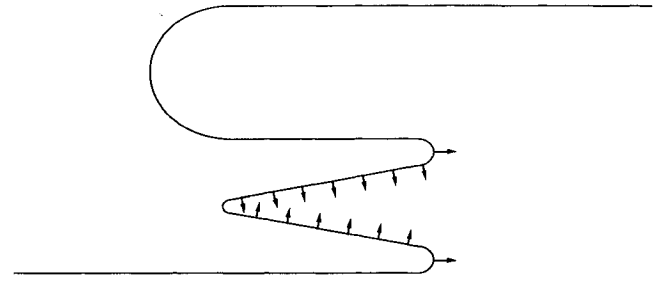

Fig. 2 Panel geometry.

Viscous Solution

The turbulent jets and the mixed flow within the ejector are treated under the thin shear layer approximation. This formulation leads to the boundary-layer equations

$$\frac{\partial u}{\partial x} + \frac{\partial v}{\partial y} = 0 \tag{1}$$

$$u\frac{\partial u}{\partial x} + v\frac{\partial u}{\partial y} + \frac{1}{\rho}\frac{\partial p}{\partial x} = \frac{1}{\rho}\frac{\partial \tau}{\partial y} \tag{2}$$

The transverse momentum equation is retained in the following approximate form[15] that relates the lateral pressure gradient to the centrifugal force associated with curved particle trajectories:

$$-\frac{\partial p}{\partial y} = \frac{\rho u^2}{R} \tag{3}$$

An approximate solution to Eqs. (1-3) is obtained by assuming the following general solution forms (denoted by hats) for the velocity and pressure profiles within the ejector:

$$\hat{u}[c_j(x),y] = u_0(x) + 1/2a(x)[\tanh(\eta + \eta_1) - \tanh(\eta - \eta_1)] + u_1(x)[\operatorname{sech}^2(\eta + \eta_1) + \operatorname{sech}^2(\eta - \eta_1)] \tag{4}$$

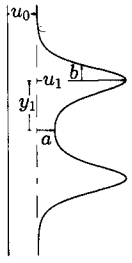

Fig. 3 Velocity profile for the dual-jet ejector.

$$\hat{p}[c_j(x),y] = \bar{p}(x) - 1/2\rho a(x)[u_0(x) + 1/2a(x)][\tanh(\eta + \eta_1) - \tanh(\eta - \eta_1) - 1] \quad (5)$$

where

$$\eta = \frac{\sigma y}{b(x)}, \qquad \eta_1 = \frac{\sigma y_1(x)}{b(x)}, \qquad \sigma = \cosh^{-1}(\sqrt{2}) \quad (6)$$

and where the average pressure $\bar{p}(x)$ is defined as

$$\bar{p}(x) = p_{\text{atm}} - 1/2\rho\left[u_0(x)^2 + u_0(x)a(x) + 1/2a(x)^2\right] \quad (7)$$

Although these profiles have some resemblance to the well-known self-similar solution for freejets, it should be emphasized that these profiles are by no means self-similar. A great deal of flexibility is available from the six degrees of freedom provided by the scaling functions $c_j(x) = [u_0(x), u_1(x), \bar{p}(x), a(x), b(x), y_1(x)]$ (see Fig. 3). If a self-similar solution existed for this flow, these scaling functions would be rigidly predetermined. In contrast, the scaling functions are determined in the present method by imposing the conditions that mass, momentum, and kinetic energy be conserved on a global basis within the viscous region and that the viscous and inviscid solutions match at the interface between them. Unlike a self-similar solution, the scaling functions used here must be determined for each ejector geometry to account properly for the influence of the secondary flow on the jet development.

The turbulent shear stress is related to the mean velocity gradient via the Bussinesq approximation

$$\frac{1}{\rho}\tau = \nu_t \frac{\partial u}{\partial y} \quad (8)$$

The eddy viscosity coefficient is determined algebraically through the following scaling hypothesis:

$$\nu_t = k u_1 b \quad (9)$$

where $k = 0.0283$ is an empirical constant that is derived from the experimentally observed spreading rate of freejets.[16] It should be emphasized that the above choice for k does not restrict the jet spreading rate to be identical to that of a freejet. The spreading rate db/dx is determined by conservation of mass, momentum, and kinetic energy consistent with the assumed solution form and the imposed secondary flow. Use of the above value of k merely enforces the plausible assumption that momentum is diffused within the confined jet under the same relative scaling as for freejets. Without more precise and extensive experimental data for the turbulence stresses in confined jets, it is probably not worthwhile to use a more sophisticated description for k.

With the velocity, pressure, and turbulent stress profiles chosen as given above, the original problem is reduced to one of determining the scaling functions $c_j(x)$. A set of ordinary differential equations for the $c_j(x)$ can be formed by requiring a global balance of mass, momentum, and energy within the viscous region. This is done by first writing the streamwise momentum equation with v rewritten as a function of u via the continuity equation

$$\Gamma\{u,p\} = u\frac{\partial u}{\partial x} - \frac{\partial u}{\partial y}\int_0^y \frac{\partial u}{\partial x}dy + \frac{1}{\rho}\frac{\partial p}{\partial x} - \frac{1}{\rho}\frac{\partial \tau}{\partial y} = 0 \quad (10)$$

where the operator Γ is a symbolic representation of the momentum equation introduced to make the following derivation more compact. The approximate profiles are substituted into the momentum equation and the result integrated across the width of the viscous region (of generic extent y_l to y_u) along with a sequence of weighting functions $w_i(x,y)$

$$\int_{y_l}^{y_u} w_i(x,y)\Gamma\{\hat{u},\hat{p}\}\,dy = 0 \quad (11)$$

This operation leads to the following set of ordinary differential equations:

$$A_{ij}\dot{c}_j = b_i \quad (12)$$

where

$$A_{ij} = \int_{y_l}^{y_u} w_i(x,y)q_j(x,y)dy \qquad b_i = \frac{1}{\rho}\int_{y_l}^{y_u} w_i(x,y)\frac{\partial \tau}{\partial y}dy \quad (13)$$

and

$$q_j(x,y) = \hat{u}\frac{\partial \hat{u}}{\partial c_j} - \frac{\partial \hat{u}}{\partial y}\int_0^y \frac{\partial \hat{u}}{\partial c_j}dy + \frac{1}{\rho}\frac{\hat{p}}{\partial c_j} \quad (14)$$

By taking $w = 1$, a global conservation of momentum is assured; by taking $w = \hat{u}$, a global balance of kinetic energy is assured. Where needed, additional equations can be generated by choosing $w_i = q_i$. These additional equations serve to minimize the local error within the ejector channel in a least-squares sense.[14]

Mass conservation is enforced by requiring that the transverse velocity at the edge of the viscous region equal some known boundary value. For the upper boundary, this condition may be stated as

$$v(x,y_u) = -\int_0^{y_u}\frac{\partial \hat{u}}{\partial x}dy = -\dot{c}_j\int_0^{y_u}\frac{\partial \hat{u}}{\partial c_j}dy = v_u \quad (15)$$

The finer details of the viscous method for both the matching region and fully viscous region are described separately in the following two sections.

Matching Region

Within the viscous-inviscid matching region, the quantities u_0, a, and $\bar{p}$ are known from the inviscid solution (see Fig. 3). The viscous problem therefore reduces to finding solutions for u_1, b, and y_1. A further simplification is possible because the jets have not yet merged and the condition $y + y_1 \gg b$ holds everywhere in the upper half-plane.

Curvature effects associated with the jet deflection are most easily treated if a transformation is made to a curvilinear coordinate system that is locally tangent to the jet centerline. When considering the jet that lies in the upper half-plane, the following transformation is used:

$$x \to s, \qquad y - y_1 \to n \quad (16)$$

where s and n are the local stream and stream-normal directions, respectively. The above transformation is applied to Eqs. (4) and (5) along with the condition $y + y_1 \gg b$ to give

$$\hat{u}(s,n) = u_0(s) + 1/2a(s)[1 - \tanh(\zeta)] + u_1(s)\operatorname{sech}^2(\zeta) \quad (17)$$

$$\hat{p} = \bar{p}(s) + 1/2\rho a(s)[u_0(s) + 1/2a(s)]\tanh(\zeta) \quad (18)$$

where

$$\zeta = \frac{\sigma n}{b} \tag{19}$$

Global conservation of momentum and kinetic energy are used to determine equations for u_1 and b. Equations (12) and (13) written in the curvilinear coordinate system with $w_1 = 1$ and $w_2 = \hat{u}$ provide the following two differential equations:

$$\dot{c}_j \int_{-\infty}^{\infty} \left[\hat{u}(s,n)\right]^{(i-1)} q_j(s,n)\,dn = \frac{1}{\rho}\int_{-\infty}^{\infty} \left[\hat{u}(s,n)\right]^{(i-1)} \frac{\partial \tau}{\partial n}\,dn \qquad i = 1,2 \tag{20}$$

Note that the limits of integration are taken to be $\pm\infty$ rather than $n_{u,l} = \pm 2.5b$, which correspond to the assumed location of the viscous-inviscid interface. This is a simplification made possible by the fact that the solution profiles identically satisfy the momentum equation as $|n|/b$ becomes large (i.e., $\Gamma \to 0$ as $|n|/b \to \infty$). Contributions to the integrals die exponentially with $|n|/b$, and there is a negligible error made by including the intervals from $\pm 2.5b$ to $\pm\infty$. (The error is roughly 5% for $n_{u,l} = \pm 2.5b$ and decreases to 1% for $n_{u,l} = 3b$.) If this error is not acceptable, finite limits may be used at the expense of slightly more complicated integrated expressions.

An equation for y_1 is derived through a process identical to that used in jet-flap theory.[17] The procedure is to integrate the normal momentum equation [transformed version of Eq. (3)] across the jet layer. Assuming constant radius of curvature across the jet, this operation yields

$$\kappa \equiv \frac{1}{R} = -\frac{\Delta p}{J} \tag{21}$$

where

$$\Delta p = 1/2\rho a\,(2u_0 + a), \qquad J = \rho\int_{-2.5b}^{2.5b} u^2\,dn \tag{22}$$

The curvature of the jet centerline is also related to the derivatives of $y_1(s)$ via

$$\kappa = \frac{\ddot{y}}{(1-\dot{y}_1^2)^{1/2}} \tag{23}$$

With the definition $h = \dot{y}_1$, Eqs. (21) and (23) may be combined and then rewritten as the following two first-order differential equations that govern the jet trajectory:

$$\dot{y}_1 = h, \qquad h = -\frac{\Delta p}{J}(1-h^2)^{1/2} \tag{24}$$

When the integrations indicated in Eqs. (20) and (24) are performed, the following system of ordinary differential equations may be written for the unknown scaling functions:

$$\begin{bmatrix} a_{11} & a_{12} & 0 & 0 \\ a_{21} & a_{22} & 0 & 0 \\ 0 & 0 & 1 & 0 \\ 0 & 0 & 0 & 1 \end{bmatrix} \begin{Bmatrix} \dot{u}_1 \\ \dot{b} \\ \dot{y}_1 \\ \dot{h} \end{Bmatrix} = \begin{bmatrix} 0 & b_{12} & b_{13} \\ b_{21} & b_{22} & b_{23} \\ b_{31} & 0 & 0 \\ b_{41} & 0 & 0 \end{bmatrix} \begin{Bmatrix} 1 \\ \dot{u}_0 \\ \dot{a} \end{Bmatrix} \tag{25}$$

where

$$a_{11} = u_0 + 4/3u_1 + 1/2a$$

$$a_{12} = 1/b\,[u_1(u_0 + 2/3u_1 + 1/2a) - 1/4(1 - \ell n2/2)a^2]$$

$$a_{21} = 2u_0(u_0 + 2u_1 + a) + u_1(8/5u_1 + 2a) + 1/2a^2$$

$$a_{22} = 1/b\,\{u_1^2\,(2u_0 + 8/15u_1 + a) + 2u_0u_1(u_0 + a) + 1/2a^2[-(1 - \ell n2/2)(u_0 + 1/2a) + u_1]\}$$

$$b_{12} = -2u_1$$

$$b_{13} = -u_1 + 1/2(1 - \ell n2/2)a$$

$$b_{21} = -k\sigma^2 u_1/b(16/15u_1^2 + 1/3a^2)$$

$$b_{22} = -2u_1(2u_0 + u_1 + a) + 1/4a^2$$

$$b_{23} = -u_1(u_1 + 2u_0 + a) + (1 - \ell n2/2)a\,(u_0 + 1/2a) + 1/8a^2$$

$$b_{31} = h$$

$$b_{41} = \frac{-1/2a(2u_0 + a)}{2b/\sigma[\tfrac{2}{3}u_1^2 + 2u_0u_1 + u_1a - \tfrac{1}{4}a^2 + (u_0^2 + u_0a + \tfrac{1}{2}a^2)2.5\sigma]} \times [1 - h^2]^{1/2} \tag{26}$$

Note that Eq. (7) has been used to eliminate $\dot{\bar{p}}$ in favor of $\dot{u}_0$ and $\dot{a}$. The above system of equations is solved by marching in the streamwise direction with a fourth-order Runge-Kutta algorithm. Initial conditions supplied at the jet origin are the jet momentum flux (a combination of u_1 and b), jet position (y_1), and jet tilt ($\dot{y}_1 = h$). Initial values for u_0 and a, as well as boundary values for u_0, a, $\dot{u}_0$, and $\dot{a}$ along the zonal interface are found from the inviscid solution.

Mass conservation within the matching region is assured by requiring that $v_{vis} = v_{inv}$ at the zonal interface. Because this constraint is also the matching condition for the viscous-inviscid interaction, it is not imposed directly on the viscous solution. What is done, rather, is to compare v_{vis} and v_{inv} after the jet and inviscid flow are computed. Errors in mass conservation are then used to improve the guess for the inviscid panel suction velocities. The normal component of velocity within the matching region is found from the transformed version of Eq. (15)

$$v = -b/\sigma\{\zeta\dot{u}_0 + \tanh(\zeta)\dot{u}_1 - 1/2(\ell n\cosh(\zeta) - \zeta)\dot{a} + 1/b\,[u_1\zeta\tanh^2(\zeta) + (u_1 + 1/2a\,\zeta)\tanh(\zeta) - 1/2a\,\ell n\cosh(\zeta) - u_1\zeta]\dot{b}\} \tag{27}$$

Fully Viscous Region

Within the fully viscous region, it is assumed that the pressure has become uniform across the channel. This is expected to be a good approximation downstream of the jet merger since the viscous flow, now filling the channel, is constrained to flow more or less parallel to the ejector walls. Within the jet merging region, however, the annihilation of transverse momentum results in a pressure bulge near the center of the channel. Since this effect is not modeled, the present method should be restricted to configurations where the jets merge at a relatively shallow angle.

With the pressure assumed to be uniform, the jet trajectories are sensibly flat, and it is appropriate to return to a Cartesian coordinate system. The velocity profile is given by Eq. (4), and the pressure profile reduces to

$$\hat{p}(x,y) = \bar{p}(x) \tag{28}$$

Within the fully viscous region, six equations are needed to solve for the scale functions u_0, u_1, $\bar{p}$, a, b, and y_1. One

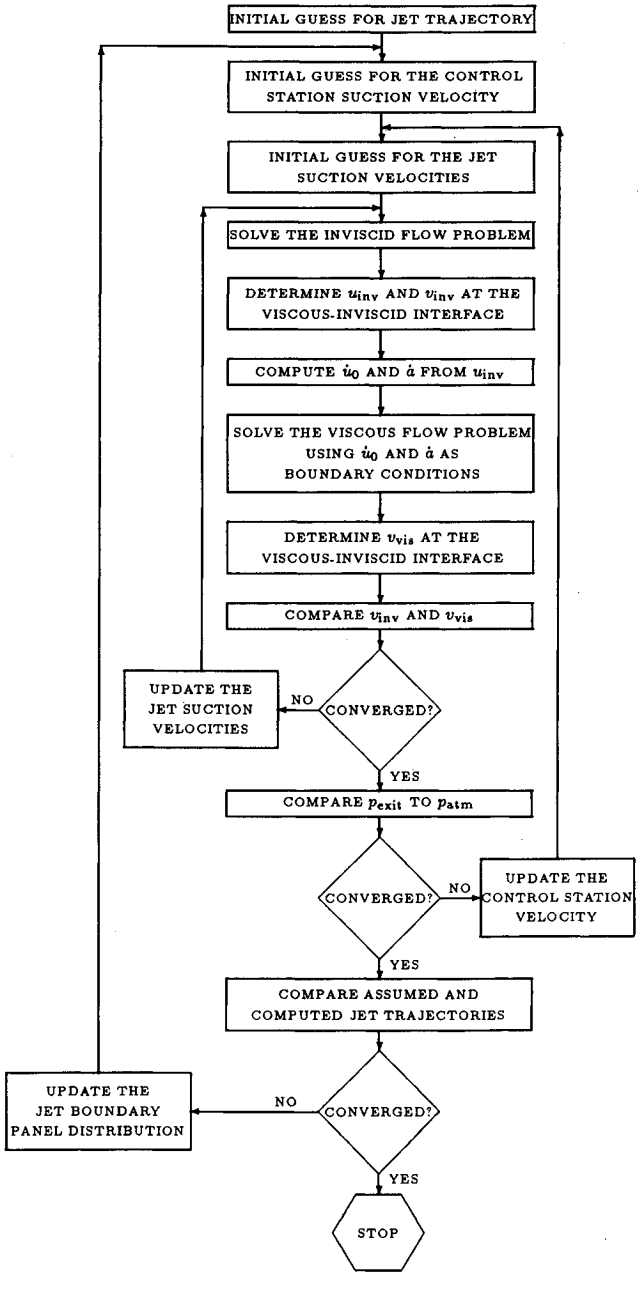

Fig. 4 Iteration scheme.

equation is obtained from Eq. (15), which enforces conservation of mass by requiring the flow to be tangent to the ejector wall

$$v(x,y=H) = -\dot{c}_j \int_0^H \frac{\partial \hat{u}}{\partial c_j} dy = \hat{u}(x,y=H)\frac{dH}{dx} \tag{29}$$

The remaining five equations are obtained from Eqs. (12) and (13), which insure a global conservation of momentum and kinetic energy as well as the condition that the local error be minimized

$$\dot{c}_j \int_0^H w_i(x,y) q_j(x,y) dy = \frac{1}{\rho}\int_0^H w_i(x,y)\frac{\partial \tau}{\partial y} dy \tag{30}$$

where $w_1 = 1$, $w_2 = \hat{u}, w_3 = q_{u_1}$, $w_4 = q_a$, and $w_5 = q_b$. Other elements of q_j could be chosen for w_3, w_4, and w_5, but these three were found to provide a slightly better conditioned set of equations.

The elements of q_j are derived by substituting the expressions for the approximate velocity and pressure profiles [Eqs. (4) and (28)] into Eq. (14). Let the elements of q_j be denoted as q_{u_0}, q_{u_1}, $q_{\dot{p}}$, etc.; then with the definitions

$$A_1 = \eta + \eta_1 \quad T_1 = \tanh(A_1) \quad S_1 = \operatorname{sech}^2(A_1)$$
$$Q_1 = \ell n \cosh(A_1)$$
$$A_2 = \eta - \eta_1 \quad T_2 = \tanh(A_2) \quad S_2 = \operatorname{sech}^2(A_2)$$
$$Q_2 = \ell n \cosh(A_2) \tag{31}$$

the individual terms are

$$q_{u_0} = \hat{u} - b/\sigma\eta$$
$$q_{u_1} = (S_1 + S_2)\hat{u} - b/\sigma(T_1 + T_2)\partial\hat{u}/\partial y$$
$$q_{\dot{p}} = 1$$
$$q_a = 1/2(T_1 - T_2)\hat{u} - b/2\sigma(Q_1 - Q_2)\partial\hat{u}/\partial y$$
$$q_b = 1/b[1/2a(-A_1S_1 + A_2S_2) + 2u_1(A_1T_1S_1 + A_2T_2S_2)]\hat{u}$$
$$- 1/\sigma[1/2a(-A_1T_1 + Q_1 + A_2T_2 - Q_2)$$
$$+ u_1(-A_1S_1 + T_1 - A_2S_2 + T_2)]\partial\hat{u}/\partial y$$
$$q_{y_1} = \sigma/b[1/2a(S_1 + S_2) + 2u_1(-T_1S_1 + T_2S_2)]\hat{u}$$
$$- [1/2a(T_1 + T_2) + u_1(S_1 - S_2)]\partial\hat{u}/\partial y \tag{32}$$

where

$$\partial\hat{u}/\partial y = -\sigma/b[1/2a(-S_1 + S_2) + 2u_1(T_1S_1 + T_2S_2)] \tag{33}$$

The integration in Eq. (29) is performed to give

$$-b/\sigma\{\eta\dot{u}_0 + (T_1 + T_2)\dot{u}_1 + 1/2(Q_1 - Q_2)\dot{a}$$
$$+ 1/b[1/2a(-A_1T_1 + q_1 + A_2T_2 - Q_2)$$
$$+ u_1(-A_1S_1 + T_1 - A_2S_2 + T_2)]\dot{b}$$
$$+ [1/2a(T_1 + T_2) + u_1(S_1 - S_2)]\dot{y}_1\} \mid_{y=H}$$
$$= \hat{u}(x,y=H)\frac{dH}{dx} \tag{34}$$

The integrals contained in Eq. (30) are not easy to evaluate analytically. Accordingly, a Simpson's rule numerical scheme is used to perform these quadratures.

The system of equations given by Eqs. (30) and (34) is marched from the end of the viscous-inviscid matching region to the end of the duct.

Iteration Scheme

The matching process takes the form of a three-level nested iteration procedure where an inner loop matches the inviscid and viscous values of velocity at the zonal interface, a middle loop matches the ejector exit pressure to the ambient value, and an outer loop matches the panel geometry to the computed jet trajectory. Each of the three iteration loops is described separately in the following. Figure 4 outlines the procedure in schematic format.

Viscous-Inviscid Matching

The viscous-inviscid matching starts with a solution to the inviscid problem where a guess is made for both the location of the viscous-inviscid boundary and the suction velocities that simulate the jet entrainment and lowered pressure within the ejector. Next an arbitrary value of jet momentum flux is chosen (the choice is arbitrary since the gross thrust scales

directly with the primary jet momentum flux for incompressible flow), and the viscous equations [Eq. (25)] are marched from the nozzle to the end of the matching region with values of u_0, a, $\dot{u}_0$, and $\dot{a}$ taken from the inviscid solution at the zonal interface. Once the viscous solution is complete, the computed distribution of jet entrainment is compared with distribution assumed in the inviscid solution. An improved guess for the panel suction velocities is then made from

$$V_n^{n+1} = V_n^n + \omega(v_{vis} - v_{inv}) \tag{35}$$

where V_n is the panel suction velocity (normal to surface), v_{vis} and v_{inv} are the transverse velocity components computed from the viscous and inviscid solutions, respectively, and ω is a relaxation factor that varies along the length of the jet according to

$$\omega = 1 - 7/10\left(\frac{x - x_j}{x_{cs} - x_j}\right) \tag{36}$$

where x_j is the location of the jet nozzle, and x_{cs} is the location of the control station where the viscous-inviscid matching ends.

The above matching procedure is applied to both sides of the jet independently so that any asymmetries in the entrainment with respect to the jet centerline are properly modeled. The suction velocity applied at the control stations (and hence the pressure there) is held fixed during this portion of the matching process.

Exit Pressure Matching

Once the viscous and inviscid flows are matched, the remainder of the viscous solution is computed by marching Eqs. (30) and (34) from the control station to the ejector exit. The pressure computed at the ejector exit will in general differ from the ambient value since both the primary jet momentum flux and the pressure within the ejector at the control station have been chosen arbitrarily. The exit pressure is corrected by iteratively adjusting the suction velocity applied at the control stations while holding the primary jet momentum flux fixed. The control station suction velocity is updated through the following Newton-type iteration scheme:

$$u_{cs}^{n+1} = u_{cs}^n - f^n/f'^n \tag{37}$$

where

$$f^n = (p_{exit}^n - p_{atm}^n) \qquad f'^n = \frac{f^n - f^{n-1}}{u_{cs}^n - u_{cs}^{u-1}} \tag{38}$$

The viscous-inviscid matching loop is nested inside the exit pressure matching loop since the viscous and inviscid flows must be rematched following each change to the control station suction velocities.

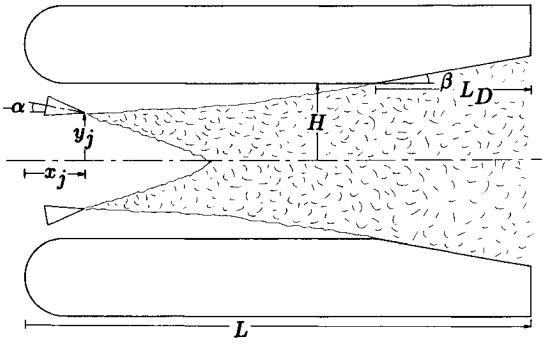

Fig. 5 Parametric variation of the ejector geometry.

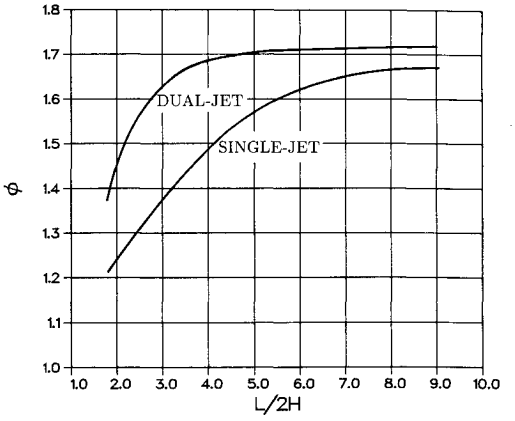

Fig. 6 Effect of the ejector length.

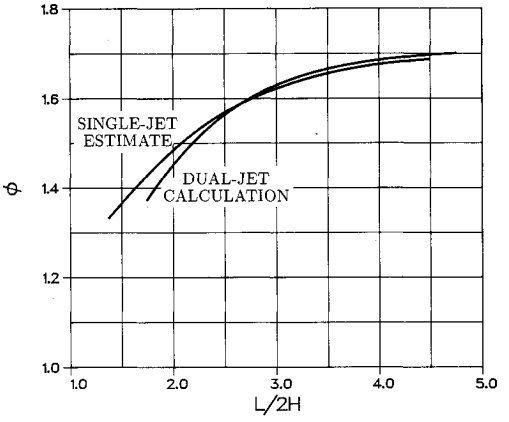

Fig. 7 Comparison of the computed results for the dual-jet ejector with an estimate based on the effective single-jet ejector concept.

Jet Trajectory Matching

The jet trajectory computed when both the viscous-inviscid matching and the exit pressure matching are complete will in general differ from the trajectory assumed at the outset. If the difference exceeds $0.05H$ at any point, the panels that simulate the jet entrainment are redistributed according to the newly computed jet trajectory, and the entire matching process is started once again.

The overall iteration scheme is illustrated in Fig. 4. The individual iteration loops converge rapidly; typically 2-3 iterations are needed to converge the exit pressure, and 2-5 iterations are needed to match the viscous and inviscid solutions.

Results and Discussion

The viscous-inviscid algorithm was used to study the relationship between ejector geometry and performance through a parametric study where various ejector parameters were independently varied. Where possible, results from the dual-jet calculations were compared with the predictions of previously developed viscous-inviscid algorithm for single-jet ejectors.[14] More extensive parametric studies as well as an optimization study for the location of the primary nozzles can be found in Ref. 14.

The ejector performance was assessed in terms of the thrust augmentation ratio, defined as the ratio of the gross ejector thrust to the thrust that would be produced by the two primary jets if they were expanded to ambient pressure

$$\phi = T_{gross}/T_0 \tag{39}$$

The gross ejector thrust was calculated by summing the momentum flux of the primary jets with the longitudinal component of the integrated surface pressure. Pressure drag associ-

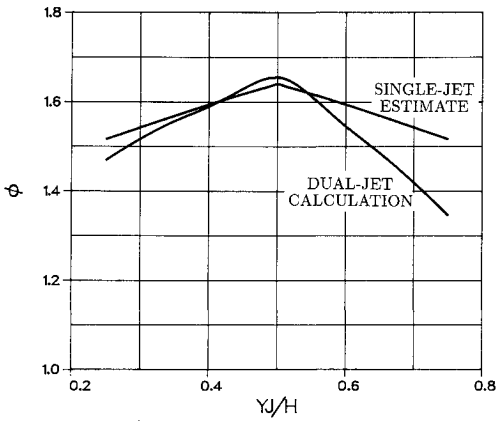

Fig. 8 Effect of the lateral nozzle position.

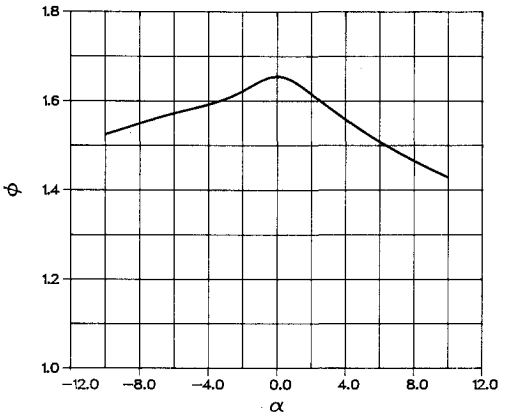

Fig. 9 Effect of the nozzle tilt.

ated with the diffuser and jet nozzles was included in the surface pressure integration. Boundary layers on the ejector walls were not modeled, and thus the results do not include skin friction. By the same token, flow separation within the diffuser was not predicted, and attached flow is assumed throughout.

Parametric Studies

Figure 5 shows the basic ejector configuration and the variable parameters. Each of the parameters was varied independently, while the others were held fixed at their nominal values $x_j/2H = 0.44$, $y_j/H = 0.5$, $\alpha = 0$, $L/2H = 3.25$, $L_D/L = 0.31$, and $\beta = 0$.

The effects of the ejector length are shown in Fig. 6. The results indicate that the performance increases monotonically with the ejector length for both the single-jet and dual-jet configurations, with higher levels of thrust augmentation present in the dual-jet case. The superior performance of the dual-jet ejector can be explained in terms of enhanced mixing resulting from an increase in the effective length of the ejector when more than one primary jet is used. It is hypothesized that the dual-jet ejector behaves like two single-jet ejectors stacked one on top of the other, with the plane of symmetry between the jets acting like a solid wall. The length to width ratio of these two effective ejectors $(L/2H)_{\text{eff}}$ is twice the original $(L/2H)$ if the jets are equispaced between the symmetry plane and the ejector wall. If the jets are not equispaced, it is expected that the effective length will be somewhat less than $2(L/2H)$. The following plausible scaling captures this effect:

$$\phi_{\substack{\text{dual}\\\text{jet}}}(L/2H, y_j/H) \simeq \begin{cases} \phi_{\substack{\text{single}\\\text{jet}}}\left[\dfrac{1}{1 - y_j/H}\left(\dfrac{L}{2H}\right)\right] & y_j/H < \tfrac{1}{2} \\ \phi_{\substack{\text{single}\\\text{jet}}}\left[\dfrac{1}{y_j/H}\left(\dfrac{L}{2H}\right)\right] & y_j/H > \tfrac{1}{2} \end{cases} \quad (40)$$

The validity of the effective ejector length concept is demonstrated in Fig. 7 where the results of the single-jet calculation are rescaled according to the above relation and plotted along with the direct dual-jet calculation. The agreement is seen to be quite good over the entire range of lengths with only a slight discrepancy for the shortest ejectors. This result suggests that a reasonable estimate of dual-jet ejector performance may be obtained by simply rescaling numerical or experimental data for a single-jet configuration.

The effect of the lateral nozzle position is illustrated in Fig. 8 where the results of the dual-jet calculation are again plotted along with the rescaled results for the single-jet configuration. Both the direct calculation and the effective single-jet estimate indicate a maximum for the symmetrical placement $y_j/$

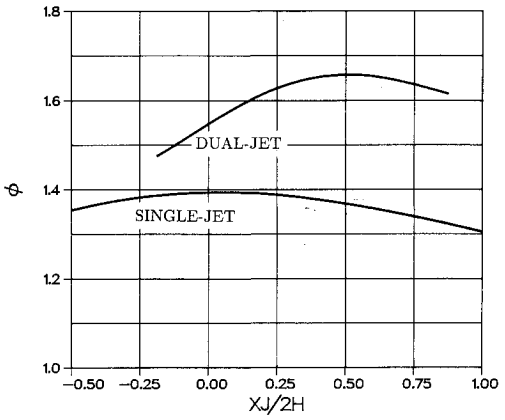

Fig. 10 Effect of the longitudinal nozzle position.

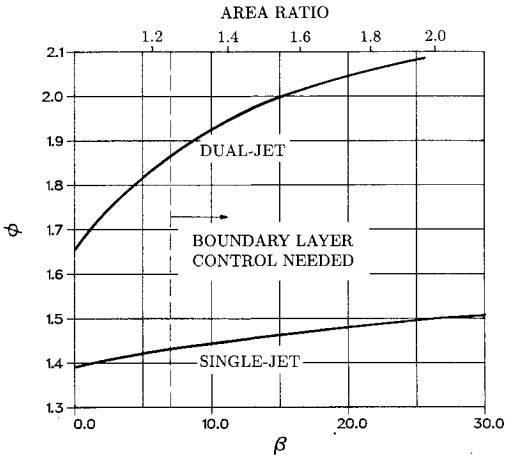

Fig. 11 Effect of the diffuser angle.

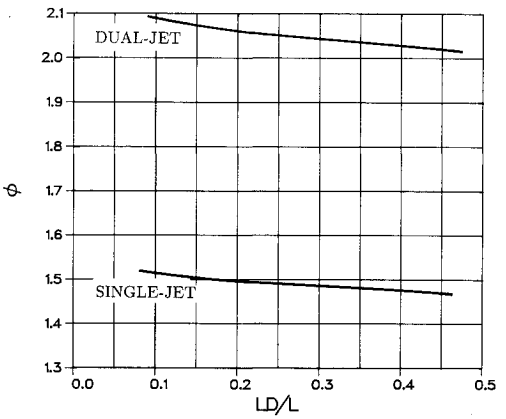

Fig. 12 Effect of the diffuser length for a constant diffuser area ratio of 1.73.

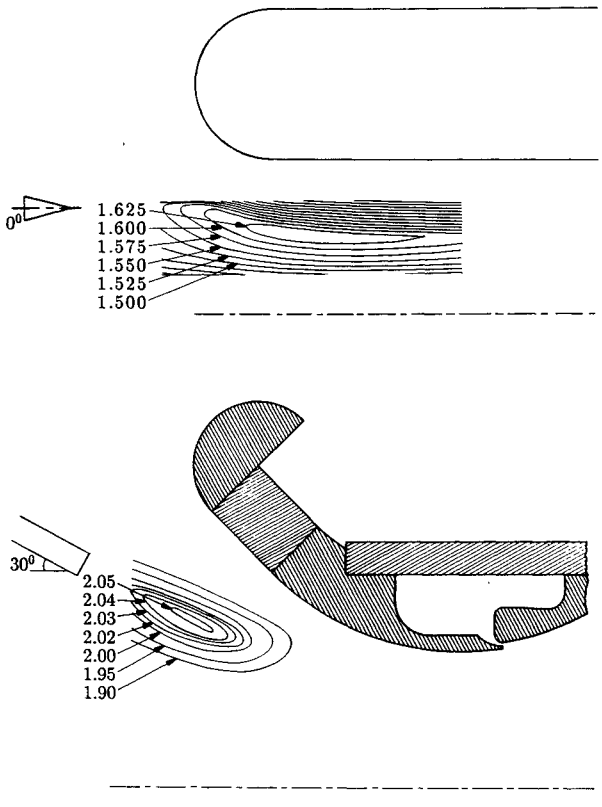

Fig. 13 Qualitative comparison with experiment; computation: $\alpha=0$, $L/2H=3.25$, $L_d/L=0$, $\beta=0$; experiment: $\alpha=-30$ deg, $L/2H=3.25$, $L_D/L=0.58$, $\beta=45$ deg, jet exit Mach number 0.56.

$H=0.5$. In contrast to the single-jet estimate, however, the direct calculation shows that the performance drops off faster when the jet is moved towards the ejector wall than when it is moved towards the channel centerline. This effect is probably caused by a reduction in turbulent mixing associated with movement of the jet into regions of increasing secondary flow velocity found near the ejector leading edge.

The effect of the nozzle tilt angle is shown in Fig. 9. The nozzle tilt angle affects the performance in much the same way as does the lateral nozzle position since issuing the jets at an angle results in a displacement of their centerlines.

The effect of the longitudinal nozzle position is shown in Fig. 10. The performance is maximized for the single-jet configuration when the nozzle is located at the entrance plane while the dual-jet configuration requires the nozzles a short distance inside the inlet. This difference illustrates the sensitivity of the dual-jet ejector performance to the alignment of the jet nozzles with respect to the streamlines of the secondary flow. Evidently the benefit realized by moving the nozzles inside the inlet to increase the alignment of the jets with the streamlines of the secondary flow outweighs the decrease in performance associated with a reduction in the distance over which the jets have to mix.

Figures 11 and 12 illustrate the effects of a diffuser. It should be kept in mind that these results were computed assuming attached boundary layers and thus do not reflect the potentially large losses associated with separated flow. For diffuser angles greater than about 7 deg, some form of boundary-layer control would most certainly be needed to achieve the theoretical predictions shown here. Figure 11 shows that the dual-jet ejector benefits more from the diffuser than does the single-jet configuration. This fact is attributed to a higher degree of mixing achieved in the dual-jet ejector upstream of the diffuser (see Ref. 14 for a control volume analysis of an ejector fitted with a diffuser). Figure 12 shows the result of a computation where the diffuser angle and length were varied simultaneously in such a way that the diffuser area ratio is held fixed. The results indicate that the performance is relatively insensitive to the details of the diffuser shape, with only a slight advantage found for a short diffuser with a large angle. This fact suggests that the diffuser design could be almost entirely based on separation considerations.

Comparison with Experiment

Predictions from the viscous-inviscid code are compared with experimental data[18] in Fig. 13. These plots show lines of constant thrust augmentation as a function of nozzle location. There is a mismatch between the two geometries because the present method, being restricted to configurations where the jets merge at a shallow angle, cannot treat the experimental configuration. In spite of the difference in geometry, the computed and experimental results share some qualitative similarities. The present method correctly predicts that the contours should be elongated in the streamwise direction and that they should be roughly aligned with streamlines of the secondary flow. The level of thrust augmentation is significantly higher in the experimental case due to the use of hypermixing nozzles as well as a high area ratio diffuser.

A more complete set of comparisons with experiment for the single jet algorithm, including velocity profile development and pressure evolution, can be found in Ref. 14.

Conclusions

A viscous-inviscid interaction methodology has been developed as an accurate and efficient means of evaluating the performance of two-dimensional incompressible flow ejectors that utilize two primary jets. The inviscid portion of the flowfield is modeled with a higher-order panel method, whereas an integral method is used to solve for the viscous jet flow. The viscous and inviscid solutions are matched together in an iterative process that simulates the interaction between the jets and the ambient fluid. Predictions of the method agree qualitatively with experimental data. The entire solution process requires under 3 min of processor time on a VAX-11/785 machine.

The algorithm has been used in a parametric study that explored the relationship between the ejector geometry and performance. Comparisons between the computed results for the dual-jet configuration and an otherwise identical single-jet configuration indicate that the dual-jet configuration consistently yields better performance. This fact can be explained in terms of an increase in the effective length of the ejector that results from the plane of symmetry between the two jets.

Acknowledgment

This research was funded by NASA Grant NCC2-390.

References

[1]Von Karman, T., "Theoretical Remarks on Thrust Augmentation," *Reissner Anniversary Volume: Contributions to Applied Mechanics,* edited by J. W. Edwards, Polytechnic Inst. of Brooklyn, Ann Arbor, MI, 1949, pp. 461-468.

[2]Keenan, J. H., Neumann, E. P., and Lustwerk, F., "An Investigation of Ejector Design by Analysis and Experiment," *Journal of Applied Mechanics,* Vol. 17, No. 3, 1950, pp. 299-309.

[3]Quinn, B., "Wind Tunnel Investigation of the Forces Acting on an Ejector in Flight," Aerospace Research Lab., Wright-Patterson AFB, OH, ARL-70-0141, July 1970.

[4]Nagaraja, K. S., Hammond, D. L., and Graetch, J. E., "One-Dimensional Compressible Ejector Flows," AIAA Paper 73-1184, Nov. 1983.

[5]Gilbert, G. B., and Hill, P. G., "Analysis and Testing of Two Dimensional Slot Nozzle Ejectors with Variable Area Mixing Sections," NASA CR-2251, May 1973.

[6]Hedges, K. R., and Hill, P. G., "Compressible Flow Ejectors—I Development of a Finite Difference Flow Model," *Transactions of the AMSE, Journals of Fluids Engineering,* Vol. 96, No. 3, 1974, pp. 272-288.

[7]Croft, D. R., and Lilley, D. G., "Finite Difference Performance Analysis of Jet Pumps," *AIAA Journal,* Vol. 14, No. 10, 1976, pp. 1347-1348.

[8]DeJoode, A. D., and Patankar, S. V., "Prediction of Three-Dimensional Turbulent Mixing in an Ejector," *AIAA Journal,* Vol. 16, No. 2, 1978, pp. 145-150.

[9]Bevilaqua, P. M., and DeJoode, A. D., "Viscid/Inviscid Interaction Analysis of Thrust Augmenting Ejectors," *Workshop on Thrust Augmenting Ejectors,* NASA CP-2093, Sept. 1979.

[10]Tavella, D. A., and Roberts, L., "Simple Viscous-Inviscid Aerodynamic Analysis of Two-Dimensional Ejectors," *Journal of Propulsion and Power,* Vol. 3, No. 5, 1987, pp. 467-471.

[11]Lund, T. S., Tavella, D. A., and Roberts, L. "Thrust Augmentor Inlet Optimization," *Journal of Propulsion and Power,* Vol. 2, No. 3, 1986, pp. 253-258.

[12]Porter, J. L., and Squyers, R. A., "A Summary/Overview of Ejector Augmentor Theory and Performance," Vought Corp., Dayton, OH, ATC Rept. R-91100/9CR-47A, 1981.

[13]Hess, J. L., "Higher Order Numerical Solution of the Integral Equation for the Two-Dimensional Neumann Problem," *Computer Methods in Applied Mechanics and Engineering,* Vol. 2, No. 1, pp. 1-15.

[14]Lund, T. S., "A Computational Study of Thrust Augmenting Ejectors Based on a Viscous-Inviscid Approach," Ph.D. Thesis, Stanford Univ., Stanford, CA, April 1987.

[15]Van Dyke, M., "Higher Order Boundary Layer Theory," *Annual Review of Fluid Mechanics,* Parabolic Press, Stanford, CA, 1969, pp. 265-292.

[16]Tavella, D. A., and Roberts, L., "Analysis of Confined Turbulent Jets," Joint Institute for Aeronautics and Acoustics, Stanford Univ., Stanford, CA, JIAA-TR-51, Dec. 1982.

[17]Spence, D. A., "The Lift Coefficient of a Thin, Jet-Flapped Wing," *Proceedings of the Royal Society—Mathematical and Physical Sciences,* Vol. 238, Royal Society, London, Dec. 1956, pp. 46-68.

[18]Alperin, M., and Wu, J.-J., "Jet-Diffuser Ejector—Attached Nozzle Design," NASA CR-152361, May 1980.